

A Quantum Critical Point Lying Beneath the Superconducting Dome in Iron Pnictides

T. Shibauchi,¹ A. Carrington,² and Y. Matsuda¹

¹Department of Physics, Kyoto University, Kyoto 606-8502, Japan;
email: matsuda@scphys.kyoto-u.ac.jp, shibauchi@scphys.kyoto-u.ac.jp

²H. H. Wills Physics Laboratory, University of Bristol, BS8 1TL, United Kingdom;
email: a.carrington@bristol.ac.uk

Annu. Rev. Condens. Matter Phys. 2014. 5:113–35

First published online as a Review in Advance on
December 16, 2013

The *Annual Review of Condensed Matter Physics* is
online at conmatphys.annualreviews.org

This article's doi:
10.1146/annurev-conmatphys-031113-133921

Copyright © 2014 by Annual Reviews.
All rights reserved

Keywords

antiferromagnetic fluctuations, unconventional superconductivity,
strongly correlated electron systems, iron-based superconductors,
quantum phase transition

Abstract

Whether a quantum critical point (QCP) lies beneath the superconducting dome has been a long-standing issue that remains unresolved in many classes of unconventional superconductors, notably cuprates, heavy fermions, and, most recently, iron pnictides. The existence of a QCP may offer a route to understanding the origin of unconventional superconductors' anomalous non-Fermi liquid properties, the microscopic coexistence between unconventional superconductivity and magnetic or some other exotic order, and, ultimately, the mechanism of superconductivity itself. The isovalent substituted iron pnictide $\text{BaFe}_2(\text{As}_{1-x}\text{P}_x)_2$ offers a new platform for the study of quantum criticality, providing a unique opportunity to study the evolution of the electronic properties in a wide range of the phase diagram. Recent experiments in $\text{BaFe}_2(\text{As}_{1-x}\text{P}_x)_2$ have provided the first clear and unambiguous evidence of a second-order quantum phase transition lying beneath the superconducting dome.

1. INTRODUCTION

The discovery of iron-pnictide high- T_c superconductivity has been one of the most exciting recent developments in condensed matter physics. In 2006, Hideo Hosono's research group found superconductivity below 6 K in LaFePO (1). They discovered that by replacing phosphorus with arsenic and doping the structure by substituting some of the oxygen atoms with fluorine, they could increase T_c to 26 K (2). This high T_c in LaFeAs(O,F) aroused great interest in the superconductivity community, particularly when it was found that T_c could be increased to 43 K with pressure (3). By the end of April 2008, it was found that T_c could be increased to 56 K by replacing La with other rare-earth elements (4). Thus, iron pnictides joined the cuprates and became a new class of high- T_c superconductor.

The most important aspect of the iron pnictides may be that they open a new landscape in which to study mechanisms of unconventional pairing that lead to high- T_c superconductivity (5–11). The high transition temperatures in both cuprates and iron pnictides cannot be explained theoretically by the conventional electron-phonon pairing mechanism, and thus there is almost complete consensus that the superconductivity of both systems has an unconventional origin (9, 12). Another class of materials in which there is extensive evidence for unconventional superconductivity is the heavy-fermion compounds (13). The unusual properties of these materials originate from the f electrons in the Ce (4*f*) or U (5*f*) atoms, which interact with the conduction electrons to give rise to heavy effective electron masses (up to a few hundred to a thousand times the free electron mass) through the Kondo effect.

There are several notable similarities between these three classes of unconventional superconductor. First of all, it is widely believed that in all three systems electron correlation effects play an important role for the normal-state electronic properties as well as the superconductivity. As in high- T_c cuprates and some of the heavy-fermion compounds, superconductivity in iron pnictides emerges in close proximity to the antiferromagnetic (AFM) order, and T_c has dome-shaped dependence on doping or pressure. In these three systems near the optimal T_c composition, various normal-state quantities often show a striking deviation from conventional Fermi liquid behavior.

Structurally, iron pnictides also have some resemblance to cuprates: Pnictides are two-dimensional (2D) layered compounds with alternating Fe-pnictogen (Pn) layers sandwiched between other layers that either donate charge to the Fe-Pn layers or create internal pressure. However, there are also significant differences between the three systems. For example, the parent compounds of the iron pnictides are metals, whereas for cuprates they are Mott insulators. Moreover, whereas in cuprates the essential physics is captured by a single band originating from a single d -orbital per Cu site, iron-based superconductors have six electrons occupying the nearly degenerate $3d$ Fe orbitals, indicating that the system is intrinsically multiorbital and therefore that the interorbital Coulomb interaction plays an essential role. Indeed, it is thought that orbital degrees of freedom in pnictides give rise to a rich variety of phenomena, such as nematicity and orbital ordering (14–30). In cuprates, a crucial feature of the phase diagram is the mysterious pseudogap phase (31–38). At present, it is not established whether an analogous phase exists in iron pnictides.

In heavy-fermion compounds, the f electrons, which are localized at high temperature, become itinerant at low temperature through Kondo hybridization with the conduction electrons. Their resultant Fermi surfaces usually have a complicated three-dimensional structure, and the competition of various interactions arising from Kondo physics also often complicates their magnetic structures. In these materials, orbital physics is important, giving rise to multipolar ordering, which is analogous to orbital ordering in a d -electron system (39), but often the nature of multipolar

ordering is not so simple because of the complicated Fermi surface and strong spin-orbit interactions. Iron pnictides, in sharp contrast, have much simpler quasi-2D Fermi surfaces with weaker spin-orbit interactions and simple magnetic structures (40), and therefore in these latter materials the physics of the critical magnetic fluctuations should potentially be easier to understand.

A quantum critical point (QCP) is a special class of second-order phase transition that takes place at absolute zero temperature, typically in a material in which the phase transition temperature has been driven to zero by nonthermal parameters, such as doping, and the application of pressure or a magnetic field (41–46). In this short review, we address several questions concerning the physics of a putative QCP in the phase diagram of the iron-pnictide materials (47). In particular, we review the evidence for a QCP hidden beneath the superconducting dome, which we believe to be crucially important for understanding the anomalous normal-state properties and the high- T_c superconductivity. In cuprates and heavy-fermion compounds, this issue, i.e., whether the pseudogap phase or the magnetically ordered phase terminates at a QCP inside the superconducting dome, has been hotly debated but remains puzzling (48–51). Here we focus on the electronic properties of the 122 family with the parent compound BaFe_2As_2 , which is the most studied among the various families of iron-based superconductors discovered to date. This family provides a unique opportunity to study the evolution of the electronic properties over a wide range of the phase diagram, ranging from spin density wave (SDW) metal through a high- T_c superconductor to conventional Fermi liquid metal. In particular, the isovalently substituted system $\text{BaFe}_2(\text{As}_{1-x}\text{P}_x)_2$ (52) provides a particularly clean system because P-substitution does not induce appreciable scattering (53, 54).

2. QUANTUM CRITICALITY

2.1. Quantum Phase Transition

Ordinary phase transitions are driven by thermal fluctuations and involve a change between an ordered and a disordered state. At absolute zero temperature, where there are no thermal fluctuations, a fundamentally new type of phase transition can occur called a quantum phase transition (41–48, 55, 56). Quantum phase transitions are triggered by quantum fluctuations associated with Heisenberg’s Uncertainty Principle. This type of phase transition involves no change in entropy and can be accessed only by varying a nonthermal parameter—such as magnetic field, pressure, or chemical composition. When the transition is continuous, the point that separates the two distinct quantum phases at zero temperature is called a QCP. The physics of quantum criticality has become a frontier issue in condensed matter physics, in particular in strongly correlated systems.

Figure 1 illustrates a typical example of the phase diagram in the vicinity of a continuous quantum phase transition. The ground state of the system can be tuned by varying the nonthermal parameter g . The system undergoes a continuous phase transition at finite temperature T_o . In the close vicinity of T_o , there is a region of critical thermal fluctuations. With increasing g , T_o decreases. The end point of a line of this continuous finite temperature phase transition ($g = g_c$) is the QCP, at which quantum phase transition from ordered phase to disordered phase occurs at $T = 0$ K. At the QCP, two distinct states at $g < g_c$ and $g > g_c$ are mixed, and the wave function is a nontrivial superposition of the two quantum states. Approaching the QCP, the order parameter correlation length ξ and correlation time ξ_τ (i.e., the correlation length

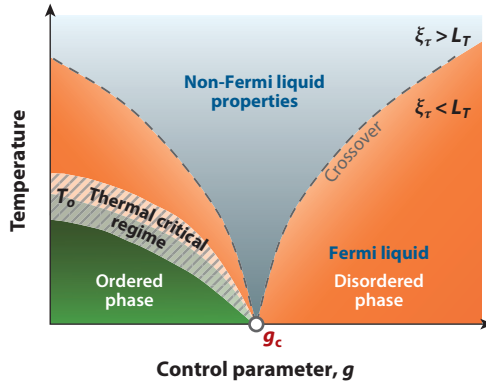


Figure 1

General phase diagram near a quantum critical point, g_c . The second-order phase transition to an ordered phase at T_o can be suppressed by a nonthermal parameter, g . At finite temperatures near T_o , a thermal fluctuation regime exists where conventional scaling properties can be observed. When approaching the quantum critical point from the right-hand side, the correlation length diverges. When the temperature is lowered toward zero, the thermal length diverges. Above the crossover line where these two length scales become comparable, a fan-shaped non-Fermi liquid region appears.

along the imaginary time axis), which characterize the dynamical (temporal) fluctuations, diverge as

$$\xi \propto |g - g_c|^{-\nu}, \quad 1.$$

where $|g - g_c|$ is the distance to the QCP, and ν is the correlation length exponent, and

$$\xi_\tau \propto \xi^z, \quad 2.$$

where z is the dynamical exponent of the quantum phase transition (41, 44, 45). The dispersion relation at the QCP is $\omega \propto k^z$: $z = 1$ for AFM localized spin systems with spin wave excitations, and $z = 2$ for itinerant AFM systems. At a finite temperature in a quantum system, there is a finite timescale,

$$L_\tau = \frac{\hbar}{k_B T}, \quad 3.$$

which characterizes the thermal fluctuations (i.e., thermal length along the imaginary time axis).

The disordered phase of the system at finite temperature can be divided into distinct regimes: $L_\tau > \xi_\tau$ and $L_\tau < \xi_\tau$. The dashed lines in **Figure 1** represent the crossover line defined by $\xi_\tau = L_\tau$ or $T \propto |g - g_c|^{\nu z}$. For the low-temperature regime $L_\tau \gg \xi_\tau$, the thermal timescale is much longer than the quantum timescale. In this regime, excitations from the quantum ground state are only weakly influenced by the thermal fluctuations and hence the system can be described by the ground state wave function. The quasiparticle excitations are well defined, and the temperature dependence of the physical quantities can be calculated by the thermal average of independent quasiparticles. For itinerant electron systems, the temperature dependence of the physical quantities exhibits conventional Fermi liquid behavior, such as T^2 -dependence of the resistivity, T -independent electronic specific-heat coefficient γ [where $\gamma(T) \equiv C_e(T)/T$ and $C_e(T)$ is the electronic contribution to the specific heat], and T -independent magnetic susceptibility χ .

However, the high-temperature regime above the QCP exhibits a completely different behavior. In this regime, where the thermal timescale is much shorter than the quantum timescale ($L_\tau \ll \xi_\tau$), the physical properties at finite temperatures are seriously influenced by the presence of the QCP at $g = g_c$: The system in this regime cannot be simply described by the ground state wave function at g . In this quantum critical regime, the temperature dependence of the physical quantities often exhibits a striking deviation from conventional Fermi liquid behavior. For instance, in the 2D case the resistivity shows a T -linear behavior at low temperature, $\rho \propto T$, and $\gamma(T)$ and $\chi(T)$ become strongly temperature dependent with divergent behavior, as $T \rightarrow 0$ K, $C_e/T \propto \log T$ (for the 3D case, $\rho \propto T^{3/2}$ and $C_e/T \propto \text{constant} - \sqrt{T}$) (57).

The dashed crossover lines in **Figure 1** border the region of quantum critical fluctuations. The quantum critical region has a characteristic fan shape. Remarkably, and somewhat paradoxically, the importance of quantum criticality expands with increasing temperature, far beyond the isolated QCP at $T = 0$. Thus, the quantum fluctuations originating from the QCP can extend to a finite temperature, giving rise to unusual physical phenomena.

The quantum criticality has been studied most extensively in nonsuperconducting heavy-fermion systems (46, 55, 56), such as $\text{CeCu}_{6-x}\text{Au}_x$ (58) and YbRh_2Si_2 (59), and the ruthenate $\text{Sr}_3\text{Ru}_2\text{O}_7$ (60). Here we focus on the correlated electron systems in which unconventional superconductivity emerges near the antiferromagnetic QCP.

2.2. Quantum Critical Points in Unconventional Superconductors

As mentioned above, iron pnictides and heavy-fermion compounds share common features in that unconventional superconductivity emerges in close proximity to an antiferromagnetically ordered state and a superconducting dome appears as a function of doping or pressure, with the maximum T_c found close to the extrapolated end point of the AFM transition. The situation in the cuprates is somewhat different in that T_c is small or zero close to the end point of the AFM transition. Instead, the maximal T_c , which occurs at a hole doping per Cu of $p = 0.16$, is close to the zero temperature end point of the pseudogap phase, which has been estimated to occur at approximately $p = 0.19$ (32, 33, 61). The pseudogap is characterized by a gradual depression of the density of states (DOS) at the Fermi level and a strong suppression of spin and charge excitations (31), which sets in at temperature T_{pg}^* . Recent experiments have suggested possible broken rotational and time-reversal symmetries within the pseudogap regime (34–37), supporting the view that the pseudogap state is a distinct phase. Within the pseudogap phase, there seems to be another critical point close to $p = 1/8$ where charge ordering (38, 62, 63) that leads to Fermi surface reconstruction (64) is observed. There is evidence that the effective mass increases substantially close to a critical point at $p = 0.10$ associated with this phase (65); however, the ordering that occurs here seems to correspond to a depression in T_c rather than any enhancement. So if cuprate superconductivity is also to be interpreted within the quantum critical framework, it would seem that the pseudogap phase is the best candidate for the fluctuating phase. We also note that near the optimal doping the resistivity exhibits T -linear dependence over a wide temperature range.

A major open question in these three systems is whether the QCP lies beneath the superconducting dome or whether the criticality is avoided by the transition to the superconducting state. This question is intimately related to the following three fundamental issues:

1. Are quantum fluctuations that are associated with the QCP essential for superconductivity?
2. Are the non-Fermi liquid properties in the normal state above T_c observed near the optimally doped regime driven by the quantum fluctuations?
3. Can unconventional superconductivity coexist with magnetic or some other exotic long-range order on a microscopic level?

This last issue is motivated by the fact that the existence of a QCP inside the dome suggests the presence of two distinct superconducting ground states, one of which may coexist with a magnetic state. Microscopic coexistence of superconductivity and magnetism has been a long-standing unsolved problem in heavy-fermion compounds (50, 51, 66, 67) as well as in iron pnictides (40, 68–72). In spite of intensive studies using various probes, it remains unclear whether the long-range AFM order truly coexists microscopically with superconducting regions or whether there is microscopic phase separation. So far the answer to this question seems to depend strongly on the experimental technique used to probe it. The type of coexistence we are referring to here is fundamentally different from the type observed in compounds such as Chevrel phases, borocarbides, and some heavy-fermion compounds, e.g., UPd_2Al_3 , in which the magnetism occurs in a different electronic subsystem than the main conduction electrons (73). In the present case, the same electrons are responsible for both types of behavior.

A major obstacle to probing the presence or absence of a QCP inside the superconducting dome is the presence of the superconductivity itself, which makes most experimental probes insensitive to its presence. Attempting to remove the superconductivity by, for example, using a high magnetic field, is not straightforward either. Besides the fact that very large fields (> 50 T) are required for iron pnictides, the presence of this field affects the original magnetic phase boundary in the zero-temperature limit and may drastically change the nature of the quantum critical fluctuations.

Figure 2a–c illustrates several possible generic temperature versus nonthermal control parameter phase diagrams for heavy-fermion compounds and iron pnictides:

1. Case A: A repulsion between AFM and superconducting (SC) order: Quantum criticality is avoided by the transition to the superconducting state (**Figure 2a**). There is no trace of a QCP in this case. This phase diagram has been reported for CeIn_3 and CePd_2Si_2 (67).
2. Case B: The magnetic order abruptly disappears at a temperature where magnetic and superconductivity phase boundaries meet (**Figure 2b**). A first-order or a nearly first-order phase boundary appears at a composition x_1 , and there is no magnetic QCP. A nearly vertical first-order line at x_1 , which separates two phases, has been reported in CeRhIn_5 (50, 51).
3. Case C: A QCP lies beneath the superconducting dome (**Figure 2c**). The second-order quantum phase transition occurs at the QCP (x_c), and the QCP separates two distinct superconducting phases (SC1 and SC2). The point at which magnetic and superconductivity phase boundaries meet is a tetracritical point. As shown later, this phase diagram is realized in $\text{BaFe}_2(\text{As}_{1-x}\text{P}_x)_2$ (74).

Usually, when looking for a mechanism of superconductivity, we think of some form of boson-mediated pairing between two electrons to form a Cooper pair. The strength and characteristic energy of the coupling then determines T_c . However, more generally, the transition to the superconducting state takes place when the energy of the superconducting state is lower than that of the normal state it replaces. Therefore, we can view the mechanism in which quantum criticality causes superconductivity in two different ways. First, the quantum critical fluctuations enhance the bosonic coupling strength and so produce strong Cooper pairing in the usual way, i.e., similar to the enhancement that occurs in electron-phonon coupled superconductors near a structural phase transition, where a phonon branch softens and becomes strongly coupled to the electrons. Second, the increase in the normal state energy caused by the quantum fluctuations means that a transition to the superconducting state, where such excitations are gapped out, is more energetically favorable and therefore occurs at a higher temperature than normal. The pairing in this case need not necessarily be solely due to the quantum fluctuations but may involve other channels, such as phonons. These two mechanisms are not mutually exclusive, but it is natural to associate the

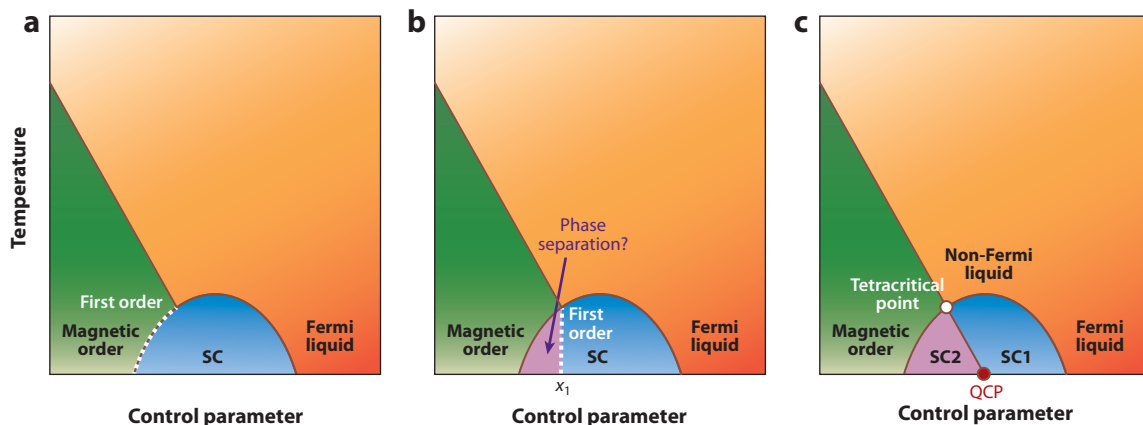


Figure 2

Three possible schematic phase diagrams with a superconducting (SC) dome near a quantum critical point (QCP). (a) The (magnetic) order competes with and cannot coexist with superconductivity. The boundary between the ordered phase and superconducting phase is the first-order phase transition. (b) Similar to the case found in panel *a* except that the first-order nature of the boundary may lead to a sizable region of phase separation up to the concentration x_1 . (c) The second-order phase transition line of the (magnetic) ordered phase crosses the superconducting transition line, and the QCP exists inside the superconducting dome. There should be two different phases inside the dome (SC1 and SC2). The SC2 phase is a microscopic coexistence phase of magnetic order and superconductivity.

former with Case C and the latter with Cases A and B. This is because when the criticality is avoided in the superconducting state (Cases A and B), the superconducting gap formation suppresses the effect of quantum fluctuations on the entropy, leading to a gain in the condensation energy.

3. 122 FAMILY

3.1. Crystal and Electronic Structure

There have now been several different types of iron-pnictide superconductors discovered. The families are often abbreviated to the ratio of the elements in their parent compositions and are known as the 111, 122, 1111, 32522, and 42622 types (6, 7). In addition, there are also iron-chalcogenide materials of the 11 and, most recently, 122' types (75), which show much of the same physics as the iron pnictides.

Crudely, the electronic and crystal structures and phase diagrams of all iron-based superconductors are quite similar. The crystals are composed of a 2D Fe layer, which is formed in a square lattice structure with an Fe-Fe distance of approximately 0.28 nm. The As (or P/Se/Te) atoms reside above and below the Fe layer, alternatively, and are located at the center of the Fe-atom squares, forming a tetrahedron FeAs_4 (Figure 3*a-c*). Because of the strong bonding between Fe-Fe and Fe-As sites, the geometry of the FeAs_4 plays a crucial role in determining the electronic properties of these systems. The Fermi surface in these materials consists of well-separated hole pockets at the center of the Brillouin zone and electron pockets at the zone corners (Figures 3*d,e*). The parent compound is an SDW metal. The SDW is suppressed either by chemical substitution or by pressure. All the families exhibit a tetragonal-to-orthorhombic structural transition (i.e., broken C_4 symmetry) that either precedes or is coincident with the SDW transition.

3.2. Magnetic Structure

BaFe_2As_2 undergoes a tetragonal-orthorhombic structural transition at $T_s = 135$ K, and at the same temperature it exhibits a paramagnetic-to-SDW phase transition. The magnetic structure of

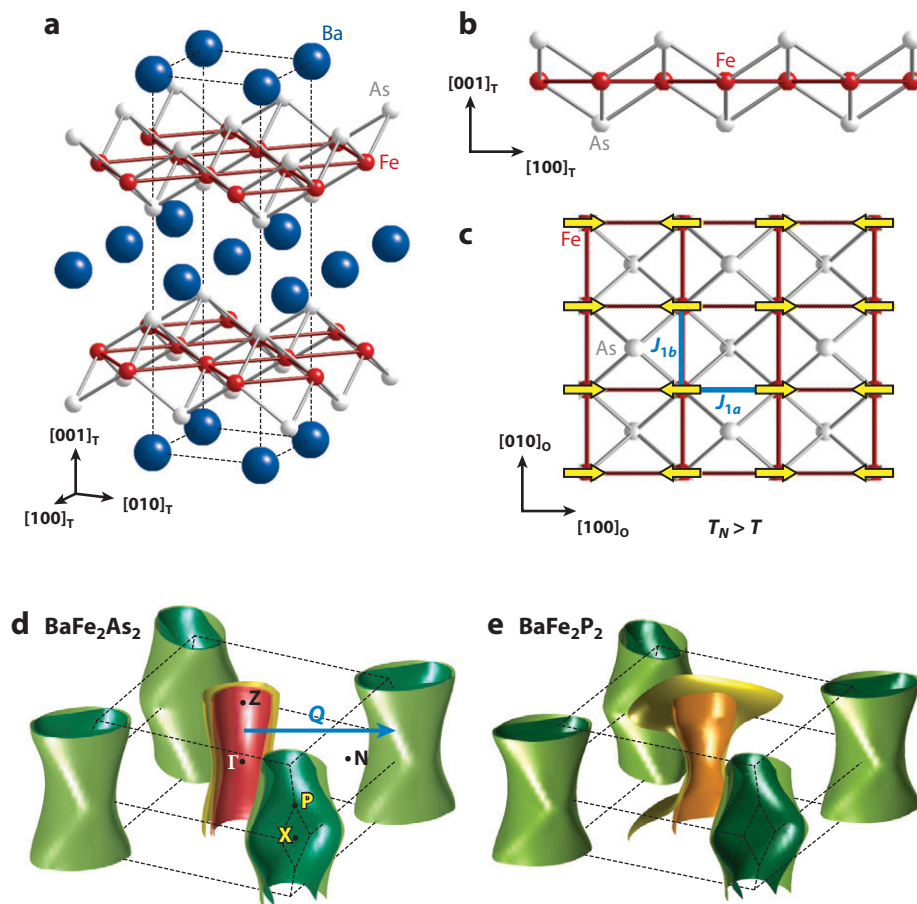


Figure 3

Crystal and electronic structure in BaFe_2As_2 . (a) Schematic crystal structure. The dotted line represents the unit cell. (b, c) The Fe-As network forms the 2D planes. The arrows in panel c illustrate the spin configuration in the antiferromagnetic state below T_N . (d) The Fermi surface structure of BaFe_2As_2 in the paramagnetic state. Three hole sheets near the zone center and two electron sheets near the zone corner are quasi-nested when shifted by vector $\mathbf{Q} = (\pi, \pi, 0)$. (e) For comparison, the Fermi surface structure of BaFe_2P_2 is also shown. The number of hole sheets is two in BaFe_2P_2 and three in BaFe_2As_2 , but in both cases it satisfies the compensation condition that the total volume of the hole Fermi surface is the same as that of the electron.

BaFe_2As_2 is collinear with a small ordered moment ($\sim 0.9\mu_B$ per Fe) (76) in which the arrangement consists of spins antiferromagnetically arranged along one direction of nearest neighbors (a axis) within the iron lattice plane and ferromagnetically arranged along the other direction (b axis) (Figure 3c). There is a small (0.7%) reduction in bond length along the direction in which the spins are ferromagnetically coupled, leading to a reduction in symmetry. A similar collinear spin structure has also been reported in other pnictides, such as AFe_2As_2 ($A = \text{Ca}$ and Sr), AFeAsO ($A = \text{La}$, Ce , Sm , Pr , etc.), and NaFeAs , whereas Fe_{1+y}Te exhibits a bicollinear spin structure (77). Inelastic neutron-scattering experiments have mapped out spin waves on single crystals of CaFe_2As_2 , SrFe_2As_2 , and BaFe_2As_2 throughout the Brillouin zone. It has been pointed out that neither localized nor itinerant models can satisfactorily describe these magnetic structures and excitation spectra (40). Recently, a possible orbital ordering has been suggested to occur

together with magnetic ordering, which lifts the degeneracy between d_{xz} and d_{yz} orbitals (19, 21). Such an orbital-ordered state has been suggested to be important to understand not only the magnetism (14, 15, 27, 40) but also the transport properties (16, 22, 23, 26, 28).

3.3. Superconductivity

High-temperature superconductivity develops when the parent AFM/orthorhombic phase is suppressed, typically by the introduction of dopant atoms. In most of the iron-based compounds, the magnetic and structural transition temperatures split with doping (6, 7). The hole doping is achieved by substitution of Ba^{2+} by K^{1+} in $(\text{Ba}_{1-x}\text{K}_x)\text{Fe}_2\text{As}_2$, and electron doping is achieved by substitution of Fe by Co in $\text{Ba}(\text{Fe}_{1-x}\text{Co}_x)_2\text{As}_2$ or Ni in $\text{Ba}(\text{Fe}_{1-x}\text{Ni}_x)_2\text{As}_2$. High- T_c superconductivity appears even for the isovalent doping with phosphorous in $\text{BaFe}_2(\text{As}_{1-x}\text{P}_x)_2$ or ruthenium in $\text{Ba}(\text{Fe}_{1-x}\text{Ru}_x)_2\text{As}_2$. The magnetic and superconducting phase diagrams of the BaFe_2As_2 -based systems are shown in Figure 4. In the hole doped $(\text{Ba}_{1-x}\text{K}_x)\text{Fe}_2\text{As}_2$, the structural/magnetic phase transition crosses the superconducting dome at $x \sim 0.3$, and a maximum T_c of 38 K appears at $x \cong 0.45$. Upon hole doping, the hole pocket expands and the electron pocket shrinks and disappears at $x \sim 0.6$ (78) or $x > 0.7$ (79). The superconductivity is observed even at the hole-doped end material ($x = 1$) KFe_2As_2 , which corresponds to 0.5 holes per Fe atom. In the electron-doped $\text{Ba}(\text{Fe}_{1-x}\text{Co}_x)_2\text{As}_2$, the maximum T_c of 22 K appears at $x = 0.07$. In contrast to the hole-doped case, superconductivity vanishes at only 0.15 electrons per Fe atom (although note that each

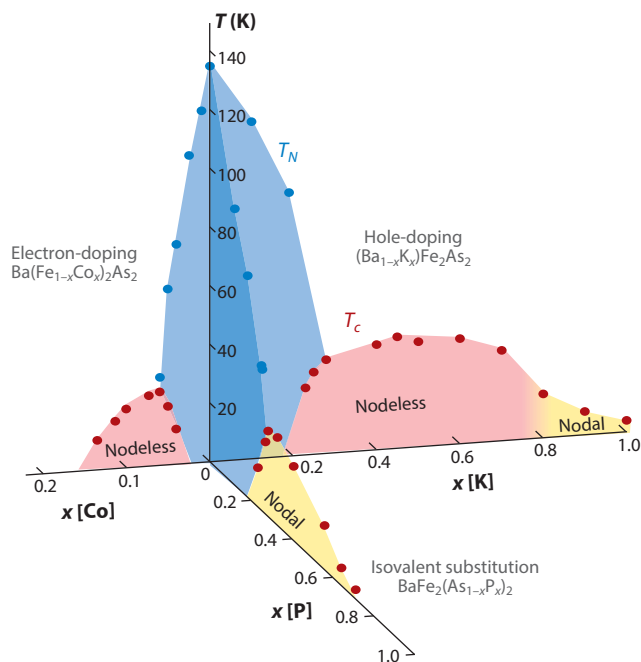


Figure 4

Magnetic and superconducting phase diagram of BaFe_2As_2 -based materials. Superconductivity emerges when the AFM order is suppressed via either (*right*) hole doping in $(\text{Ba}_{1-x}\text{K}_x)\text{Fe}_2\text{As}_2$, (*left*) electron doping in $\text{Ba}(\text{Fe}_{1-x}\text{Co}_x)_2\text{As}_2$, or (*bottom*) isovalent substitution in $\text{BaFe}_2(\text{As}_{1-x}\text{P}_x)_2$. In the P-substituted system and in the overdoped region of a K-doped system, the superconducting gap has line nodes.

doped K atom adds only 0.5 holes per Fe atom). This electron-hole asymmetry in the phase diagram has been attributed to an enhanced Fermi surface nesting in the hole-doped compounds. Superconductivity with $T_c = 31$ K also appears in heavily electron-doped $A_x\text{Fe}_{2-y}\text{Se}_2$ with no hole pockets (75).

3.4. Isovalent Substitution System

The isovalently doped $\text{BaFe}_2(\text{As}_{1-x}\text{P}_x)_2$ is a particularly suitable system for studying the detailed evolution of the electronic properties because of the following reasons. In isovalent doping with no introduction of additional charge carriers, the dopant changes the electronic structure mainly because of differences in ion size. In fact, the phase diagram of $\text{BaFe}_2(\text{As}_{1-x}\text{P}_x)_2$ can be retraced with hydrostatic pressure from any starting P concentration (52), suggesting that external pressure is equivalent to chemical substitution of As by the smaller P ion. Observation of quantum oscillations in a wide x -range ($0.38 \leq x \leq 1$) demonstrates the low scattering rate of the defects introduced by P-substitution (53, 80–82), particularly for the electron sheets.

According to density function theory (DFT) band-structure calculations (52, 53), three hole sheets exist around the zone center (Γ point) in BaFe_2As_2 , whereas one of them is absent in BaFe_2P_2 (Figure 3*d,e*). Both compounds have two electron pockets around the zone corner (X point). The three dimensionality of the hole Fermi surfaces is quite sensitive to the pnictogen position z_{Pn} . The substitution of P for As reduces both the c -axis length and z_{Pn} and eventually leads to the loss of one of the hole sheets and a strong increase in the warping of another, which gains strong d_{z^2} character close to the top of the zone (Z point). This increased Fermi surface warping upon doping weakens the nesting along the (π, π) direction. In contrast to the significant changes in the hole sheets, the electron sheets are almost unchanged in the calculations, although experimentally a significant reduction in their volume is found (53).

3.5. Superconducting Gap Structure and Symmetry

Detailed knowledge of the superconducting gap structure and how it varies between different families can be useful in helping to decide between microscopic theories (9, 11, 83–89). The superconducting gap structure in the 122 family has been studied extensively by means of various experimental techniques (9). In electron-doped $\text{Ba}(\text{Fe}_{1-x}\text{Co}_x)_2\text{As}_2$, fully gapped superconductivity appears to be realized in the whole doping range (90). In hole-doped $(\text{Ba}_{1-x}\text{K}_x)\text{Fe}_2\text{As}_2$, although fully gapped superconductivity is well established in the optimally doped regime (91, 92), line nodes appear in the heavily hole-doped regime for $x \gtrsim 0.8$ (93–97, 128), where the electron pockets are absent.

In isovalently doped $\text{BaFe}_2(\text{As}_{1-x}\text{P}_x)_2$, the presence of line nodes has been reported (98–100) throughout the entire superconducting region of the phase diagram. Figure 5 shows the temperature dependence of the relative change of the London penetration depth $\Delta\lambda(T) = \lambda_L(T) - \lambda_L(0)$ down to 80 mK, as determined by a high-precision tunnel diode oscillator (operating frequency of ~ 13 MHz). For all samples measured, covering a wide range of P-concentrations, a quasi- T -linear variation of $\Delta\lambda(T)$ is observed, indicating that the presence of line nodes is a robust feature of this P-substituted system (74).

The position of the line nodes in this isovalent system has been studied extensively. There is no evidence of vertical line nodes in the hole pockets located at the zone center (101, 102), excluding a possibility of d -wave symmetry. However, whether the line nodes are present in hole or electron pockets has been controversial. Although horizontal line nodes in the hole pockets have been suggested by one ARPES (angle-resolved photoemission spectroscopy) experiment (103), loop line nodes in the electron pockets have been suggested by both a different ARPES experiment

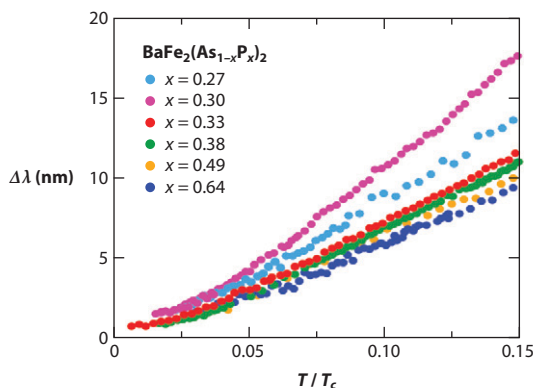


Figure 5

Relative change of the London penetration depth $\Delta\lambda$ at low temperatures plotted against T/T_c for different compositions from $x = 0.27$ to 0.64 in $\text{BaFe}_2(\text{As}_{1-x}\text{P}_x)_2$.

(102) and the angular variation of the thermal conductivity (99). It should be noted that the robustness of the line nodes against P-substitution appears to be consistent with the nodes being on the electron pockets rather than the hole pockets because the electron pockets change relatively little with x , whereas the shape of the hole sheets changes substantially (Figure 3d,e).

Recent results detailing the effect of electron irradiation on the magnetic penetration depth demonstrate that the line nodes are lifted by the impurities (Y. Mizukami, Y. Kawamoto, S. Kurata, T. Mikami, K. Hashimoto, S. Kasahara, Y. Matsuda, M. Konczykowski, C. J. van der Beek, B. Boizot, R. Prozorov, Y. Wang, A. Kreisel, V. Mishra, P.J. Hirschfeld, T. Shibauchi, unpublished results), indicating that they are not protected by symmetry (104). From the above, we conclude that the gap structure is not universal; however, the gap symmetry is universally A_{1g} , at least in the 122 family.

4. QUANTUM CRITICAL POINTS HIDDEN BENEATH THE SUPERCONDUCTING DOME

The method of isovalent substitution offers an ideal route to quantum criticality (47, 105) that is distinct from charge carrier doping or application of external pressure. Because BaFe_2As_2 exhibits SDW order and BaFe_2P_2 does not, we can place the two end materials on either side of g_c along the tuning parameter axis in the phase diagram. As x increases, the tuning parameter g increases. In this section, we discuss the presence of the QCP in $\text{BaFe}_2(\text{As}_{1-x}\text{P}_x)_2$ as evidenced by both the normal and superconducting electron responses.

4.1. Normal Electron Response

First, we discuss the normal-state properties that are studied by transport, magnetic, and thermodynamic probes as well as by quantum oscillations. These measurements are done at temperatures above T_c or at high magnetic fields above the upper critical field.

4.1.1. Transport properties. It is well established that in conventional metals the electron transport properties exhibit characteristic temperature and field dependencies, which are described by Landau's Fermi liquid theory. One of the most interesting and puzzling issues in strongly correlated

electron systems is anomalous electron transport phenomena, which often display striking deviation from Fermi liquid behavior in a wide temperature range. As shown in Figure 6a, the in-plane resistivity ρ follows the Fermi liquid relation of $\rho = \rho_0 + AT^2$ at $x \gtrsim 0.6$. In stark contrast, at $x = 0.33$, close to the optimum concentration where the maximum T_c is achieved, ρ shows linear temperature dependence, $\rho = \rho_0 + AT$ (52), which is a hallmark of non-Fermi liquid behavior. We note that along with the T -linear resistivity, a striking enhancement of the Hall coefficient at low temperatures and an apparent violation of Kohler's law for the magnetoresistance, which are both also indicative of non-Fermi liquid behavior (106), have been reported (52).

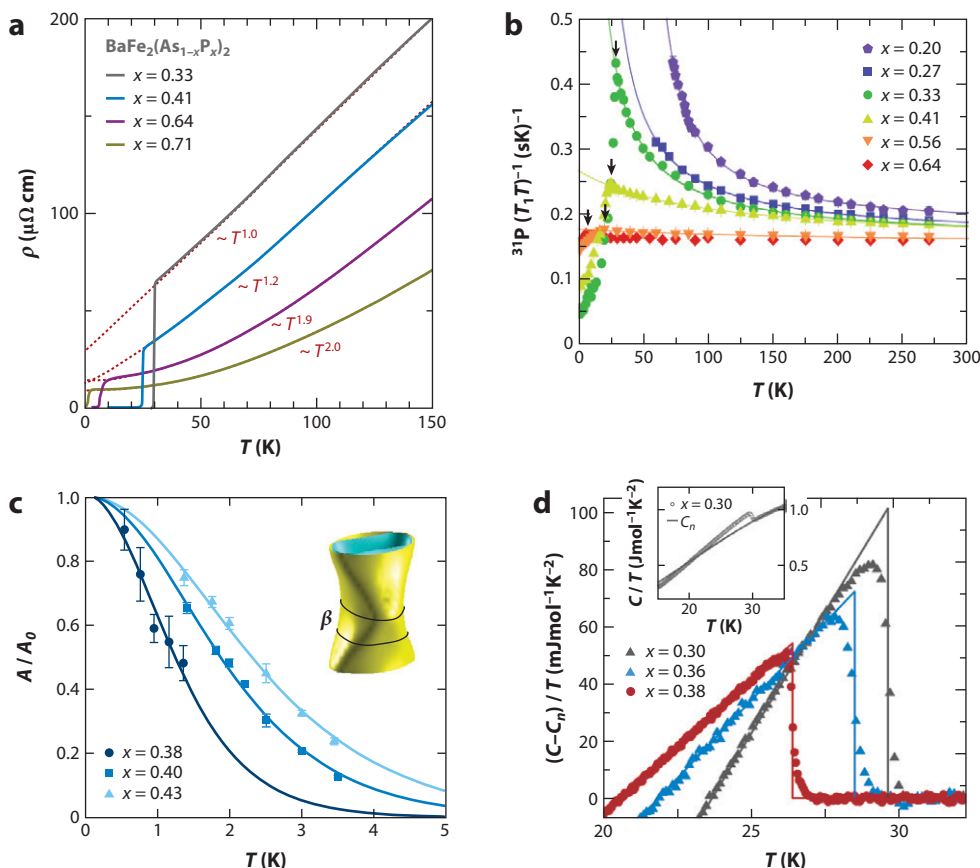


Figure 6

Quantum critical behavior of normal electrons above T_c in $\text{BaFe}_2(\text{As}_{1-x}\text{P}_x)_2$. (a) Temperature dependence of in-plane resistivity ρ for $0.33 \leq x \leq 0.71$ (52). The dashed red lines show the fit of normal-state $\rho(T)$ to power-law dependence $\rho_0 + AT^\alpha$. (b) Temperature dependence of nuclear magnetic resonance $1/T_1T$ measured for the ^{31}P nuclei for several compositions (107). The lines are the fits to the Curie-Weiss temperature dependence. (c) Temperature-dependent amplitude of a fast Fourier transform of the dHvA signal for the β orbits for samples close to the spin density wave boundary. The lines are fits to the Lifshitz-Kosevich formula. The field ranges of the fitting are from 38 T to 42 T for $x = 0.38$, 40 T to 54 T for $x = 0.40$, and 45 T to 55 T for $x = 0.43$. The inset shows extremal β orbits in the outer electron pocket. (d) The inset shows the total measured specific heat for $x = 0.30$; the solid line is the fitted normal state background C_n . The main part of the figure shows the specific heat with C_n subtracted for different values of x , and the solid lines show the entropy-conserving construction used to determine the jump height ΔC and T_c .

The color shading in **Figure 7a** represents the value of the resistivity exponent in the relation

$$\rho = \rho_0 + AT^\alpha. \quad 4.$$

A crossover from non-Fermi liquid to Fermi liquid with doping is clearly seen. The region of the phase diagram, which includes a funnel of T -linear resistivity centered on $x \approx 0.3$, bears a striking resemblance to the quantum critical regime shown in **Figure 1**. Thus, the normal state transport properties are consistent with the presence of a QCP at $x \approx 0.3$.

4.1.2. Magnetic properties. Nuclear magnetic resonance (NMR) experiments give important information about the low-energy magnetic excitations of the system. The Knight shift K and spin-lattice relaxation rate $1/T_1$ of $\text{BaFe}_2(\text{As}_{1-x}\text{P}_x)_2$ have been measured with various P concentrations (107). K is almost T -independent for all x , indicating that the DOS does not change substantially with temperature. The ^{31}P relaxation rate $1/T_1$ is sensitive to the AFM fluctuations: $1/T_1T$ is proportional to the average of the imaginary part of the dynamical susceptibility $\chi(q, \omega_0)/\omega_0$, $1/T_1T \propto \Sigma_q |A(q)|^2 \chi''(q, \omega_0)/\omega_0$, where $A(q)$ is the hyperfine coupling between ^{31}P nuclear spin and the surrounding electrons and ω_0 is the NMR frequency. In the Fermi liquid state, the Korringa relation $T_1TK^2 = \text{constant}$ holds, but it fails in the presence of strong magnetic fluctuations. In particular, AFM correlations enhance $1/T_1$ through the enhancement of $\chi(q \neq 0)$, without appreciable change of K .

Figure 6b shows the temperature dependence of $1/T_1T$ in a wide range of P-substitution. At $x = 0.64$, $1/T_1T$ is nearly temperature independent, indicating the Korringa relation $T_1TK^2 = \text{constant}$.

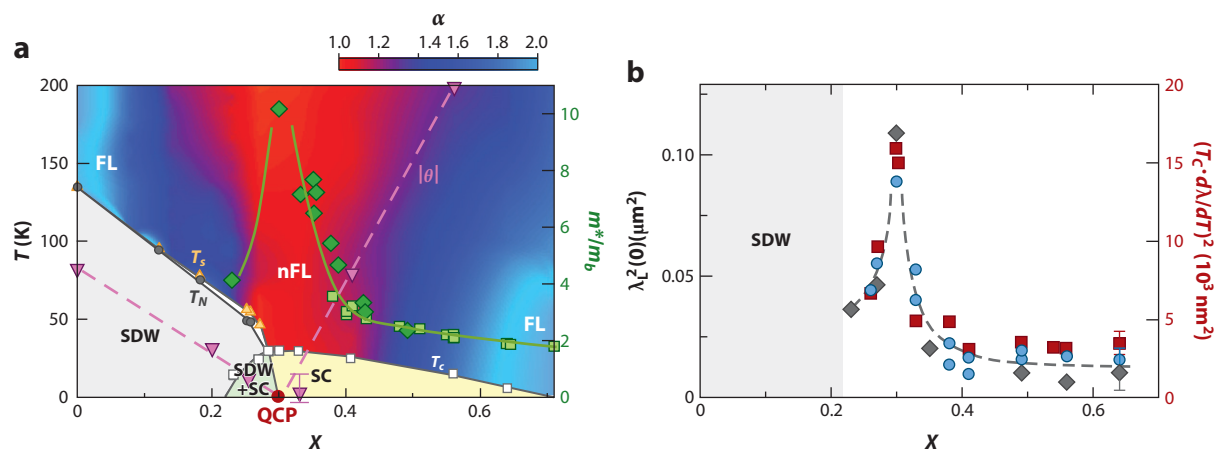


Figure 7

(a) Phase diagram of $\text{BaFe}_2(\text{As}_{1-x}\text{P}_x)_2$. Red and blue colors represent non-Fermi (nFL) and Fermi liquid (FL) regimes determined by the exponent α of the temperature dependence of the resistivity. The structural transition temperature T_s (yellow triangles), the spin density wave (SDW) transition temperature T_N (gray circles), and the superconducting (SC) transition temperature T_c (white squares) are determined by the anomalies in resistivity curves. θ is the Weiss temperature determined by the nuclear magnetic resonance relaxation rate. The light green squares and dark green diamonds represent the effective mass normalized by the band mass m^*/m_b (right axis) determined by the dHvA and specific-heat measurements, respectively. Experimental evidence for a quantum critical point (QCP) in this system at $x_c = 0.3$ includes a funnel of T -linear behavior in the resistivity centered on x_c , a steep increase in m^*/m_b as x approaches x_c , and vanishing θ at x_c . (b) The x dependence of the square of zero-temperature London penetration depth $\lambda_L^2(0)$ (74) determined by the Al-coated method (diamonds), surface impedance (circles), and slope of the temperature dependence of $\Delta\lambda_L(T)$ (squares, right axis). A sharp peak in $\lambda_L(0)$ at x_c indicates that the superfluid density is minimal at this critical x value and therefore that the QCP survives under the superconducting dome.

This Fermi liquid behavior in the magnetic properties is consistent with the transport properties. As x is varied toward the optimally doping concentration, however, $1/T_1T$ shows a strong temperature dependence, indicating a dramatic enhancement of the AFM fluctuations. It has been reported that in the paramagnetic regime, T_1 is well fitted with the 2D AFM spin fluctuation theory of a nearly AFM metal,

$$\frac{1}{T_1T} = a + \frac{b}{T + \theta}, \quad 5.$$

where a and b are fitting parameters and θ is the Curie-Weiss temperature. It has been reported that although a and b change little with x , θ exhibits a strong x dependence (107). In Figure 7a, doping evolution of $|\theta|$ is plotted. With decreasing x , θ , which is positive in the high x region, decreases and become negative in the low x region: θ goes to zero at the critical concentration $x \approx 0.3$, where non-Fermi liquid behavior in the resistivity is observed. At a second-order AFM critical point, the singular part of $1/T_1T$ is expected to vary as $1/T$, i.e., $\theta = 0$ because the dynamical susceptibility diverges at $T = 0$ K, or the magnetic correlation length continues to increase down to zero temperature. Thus, NMR experiments show that the magnetic ordering temperature approaches zero at the SDW boundary, which is consistent with the presence of a QCP at $x \approx 0.3$.

4.1.3. Fermi surface. Discovering how the Fermi surface evolves as the material is tuned from a nonsuperconducting conventional metal toward the non-Fermi liquid regime near the SDW phase boundary is an important step toward gaining a complete understanding of the mechanism that drives high- T_c superconductivity. Quantum oscillations arise from the Landau quantization of the energy levels of metals in high magnetic fields and can be used to map out the detailed Fermi surface structure. They are usually observed at very low temperatures and in very clean single crystals. The frequencies of the observed oscillations F (as a function of the inverse magnetic field) provide very accurate measurements of the Fermi surface extremal cross-sectional areas A_k via the Onsager relation $F = (\hbar/2\pi e)A_k$. The effective mass of the quasiparticles on the various orbits m^* is determined by fitting the temperature-dependent amplitude of the oscillations to the Lifshitz-Kosevich formalism. The mass enhancement, which reflects the non-mean-field electron-electron correlation effects, is given by the ratio m^*/m_b between the effective mass and the DFT calculated band mass. The quantum oscillations observed in the magnetization or torque are known as the de Haas-van Alphen (dHvA) effect.

In $\text{BaFe}_2(\text{As}_{1-x}\text{P}_x)_2$ dHvA oscillations have been observed in a wide x range (53), indicating that the substitution of As by P does not induce appreciable scattering. For the end member BaFe_2P_2 , the dHvA oscillations originating from all the Fermi surface sheets are observed and hence the complete Fermi surface is precisely determined (81). All the orbits have relatively uniform mass enhancements m^*/m_b ranging from 1.6 to 1.9 (m_b is determined by the DFT band calculation). For the As-substituted samples, the dHvA oscillations from the hole sheets are rapidly attenuated with decreasing x (53): Signals from the hole sheets have been reported only down to $x = 0.63$ (80), which is still some distance from the SDW phase boundary at which T_c reaches its maximum. However, the dHvA oscillations from the electron sheets, in particular the signals from the β orbits on the outer electron sheet (see the inset of Figure 6c), have been observed in a wide doping range up to $x = 0.38$ ($T_c = 28$ K), which is fairly close to the SDW boundary (53, 82). Figure 6c shows the temperature-dependent amplitude of the fast Fourier transform (FFT) of the dHvA signal for the β orbits for samples with different values of x near the SDW boundary. As the

SDW boundary is approached, the curve decreases more rapidly, indicating significant mass enhancement.

In **Figure 7a**, the x -dependence of m^*/m_b of the β orbit is plotted. The effective masses exhibit an upturn in samples of progressively lower P-concentration, x . The enhanced mass of the electron sheet at $x = 0.38$ reported by the ARPES (108) is quantitatively consistent with dHvA results. Concomitantly with the mass enhancement, the volume of the electron sheets (and, via charge neutrality, also the hole sheets) shrinks linearly, which is not expected from the DFT calculations (53). This implies the reduction of the Fermi temperature $T_F = \hbar v_F/m^*k_B$ with decreasing x . It is highly unlikely that these changes are a simple consequence of the one-electron band structure but instead they likely originate from many-body interactions. It is generally believed that strong quantum fluctuations near the QCP lead to a notable many-body effect, which seriously modifies the quasiparticle masses. Therefore, the enhancement in m^*/m_b and shrinkage of Fermi surface, and hence the precipitous drop of Fermi temperature as the material is tuned toward the SDW boundary, are consistent with the presence of a QCP.

4.1.4. Thermodynamic properties. As noted above, an increase in effective mass on one of the electron Fermi surfaces as the SDW boundary is approached is observed by dHvA. Specific heat measures the total DOS and so contains contributions from all the Fermi surface sheets. For BaFe_2P_2 , in which masses of almost all the observable orbits have been reported, all orbits show a relatively uniform mass enhancement, m^*/m_b . The electronic specific coefficient $\gamma = C_e/T$ is proportional to the total DOS. Because the band structure of $\text{BaFe}_2(\text{As}_{1-x}\text{P}_x)_2$ is close to the 2D limit, γ is directly proportional to m^* . Unfortunately, owing to the high superconducting transition temperatures, the direct determination of γ is extremely difficult. However, γ can be calculated by the jump of the specific heat at T_c via the relation

$$\gamma = \Delta C / \alpha_c T_c \quad 6.$$

by making the reasonable assumption that α_c , which takes the value 1.43 for weak coupling s -wave superconductors, does not change appreciably near the QCP.

Figure 6d shows $\Delta C/T$ at T_c for samples close to the SDW boundary (82). Here the anomaly at the transition ΔC has been isolated from the phonon-dominated background by subtracting a second-order polynomial fitted above T_c and extrapolated to lower temperature (see the inset of **Figure 6d**). Although there is some uncertainty in using this procedure over an extended temperature range, the lack of appreciable thermal superconducting fluctuations, as evidenced by the mean-field-like form of the anomaly, means that there is very little uncertainty in the size of ΔC . It is evident from the data that the size of the anomaly $\Delta C/T_c$ depends very strongly on x and T_c .

In **Figure 7a**, the quasiparticle mass normalized by the averaged effective mass determined by the specific heat is plotted. The average effective mass enhancement m^*/m_b is obtained by taking the ratio of γ to the band-structure value calculated by DFT for BaFe_2P_2 , $\gamma_b = 6.94 \text{ mJ}/(\text{K}^2 \cdot \text{mol})$. It should be noted that m^*/m_b estimated by the dHvA and specific-heat measurements is remarkably consistent. This quantitative agreement between the trends for mass enhancement indicated by the specific heat and dHvA results for the electron β orbits suggests that the mass enhancement is relatively uniform over the Fermi surface.

It is clear that m^*/m_b is strikingly enhanced with decreasing x and exhibits a peak at the SDW boundary: γ value reaches as large as nearly $70 \text{ mJ}/(\text{K}^2 \cdot \text{mol})$ at the boundary. Thus, the striking enhancement in effective mass with approaching SDW boundary revealed by dHvA and specific-heat measurements consistently suggest a QCP in this system at $x \approx 0.3$.

The uniform magnetic susceptibility χ is also related to the effective mass. In fact, the concomitant enhancement of γ and χ has been observed in heavy-fermion systems. However, the enhancement of the NMR Knight shift, which is proportional to $\chi(q=0)$, has not been reported near $x \approx 0.3$. The origin of this discrepancy is not understood but could be due to the inhomogeneity of the samples in NMR measurements, where collections of small crystals are used. Indeed the present specific-heat results have been obtained by using small high-quality single crystals, which are homogeneous, as shown by the sharp jump of C at T_c in **Figure 6d**, whereas previous specific-heat measurements have reported much weaker x dependence (109). Another intriguing possibility is that the nature of magnetic fluctuations near the QCP in iron pnictides may be different from that in heavy-fermion systems. The way in which the q -dependence of the dynamical susceptibility changes on approaching the QCP may be quite different in the two systems. In any case, this issue deserves further study.

4.2. Superfluid Density

Despite the bulk thermodynamic and transport signatures of quantum critical behavior of the normal quasiparticles at finite temperature, these signatures are not sufficient to pin down the location of the QCP because of the overlying superconducting dome. Because of the above-mentioned potential problem associated with destroying the superconductivity with a strong field, a direct probe that can trace across the QCP at zero temperature in zero field is desirable.

One property that directly probes the superconducting state well below T_c at zero field is the magnetic penetration depth λ_L . In the clean, local (London) limit, the absolute value of λ_L in the zero-temperature limit is given by the following expression:

$$\lambda_{L_x}^{-2}(0) = \frac{\mu_0 e^2}{4\pi^3 \hbar} \oint dS \frac{v_x^2}{|v|}, \quad 7.$$

where $\oint dS$ refers to an integral over the whole Fermi surface, and v_x and λ_{L_x} are the x components of the Fermi velocity v and the penetration depth, respectively. In a multiband system with simple Fermi surface, this may be simplified to

$$\lambda_L^{-2}(0) = \mu_0 e^2 \sum_i n_i / m_i^*, \quad 8.$$

where n_i and m_i^* are the number density (proportional to the volume) and average mass of the carriers in band i , respectively. The key point here is that λ_L is a direct probe of the normal state properties of the electrons that form the superconducting state. Measurements on very high-quality crystals are indispensable because impurities and inhomogeneity may otherwise wipe out the signatures of the quantum phase transition.

For a reliable determination of the absolute value of $\lambda_L(0)$ in small single crystals, three different methods were adopted (74). The first is the lower- T_c superconducting film coating method using a radio frequency (13 MHz) tunnel diode oscillator (110, 111). The second is the microwave cavity perturbation technique using a superconducting resonator (28 GHz) and a rutile cavity resonator (5 GHz), both of which have a high-quality factor. In the third method, $\lambda_L(0)$ is determined by the slope of T -linear dependence of $\Delta\lambda(T)$, as shown in **Figure 5**. A notable feature of the T -linear penetration depth is that the relative slope $d\Delta\lambda(T)/d(T/T_c)$ is steepest for $x = 0.30$. In general, this slope is determined by the Fermi velocity and the k -dependence of the superconducting gap close to the node. Making the reasonable assumption that the gap structure evolves weakly across the phase diagram, the x dependence of $d\Delta\lambda(T)/d(T/T_c)$ will mirror that of $\lambda_L(0)$.

Figure 7b shows the P-concentration dependence of the squared in-plane London penetration length $\lambda_L^2(0)$, which is determined by three different methods (74), in the zero-temperature limit. All three methods give very similar x dependencies. The most notable feature is the sharp peak in $\lambda_L^2(0)$ at $x = 0.30$. This striking enhancement on approaching $x = 0.30$ from either side is naturally attributed to the critical fluctuations associated with a second-order quantum phase transition, providing strong evidence for the presence of a QCP at $x = 0.30$. It should be noted that in a Galilean invariant system, such an enhancement of $\lambda_L(0)$ is not expected because the self-energy renormalization effect is canceled out by the so-called backflow correction (112). However, recent theoretical work (113, 114) has argued that in multiband systems (such as the iron pnictides), Galilean invariance is broken and the electron correlation effects give rise to a striking enhancement of the superfluid electron mass, and hence the magnetic penetration depth has a peak due to the mass enhancement at the QCP. In addition, the presence of nodes leads to a further enhancement of $\lambda_L(0)$ at the QCP (113). A very recent calculation near the QCP suggested that the exact location of the peak in $\lambda_L(0)$ may be shifted toward the SDW side (115). It has also been suggested that a strong renormalization of effective Fermi velocity due to quantum fluctuations occurs only for momenta \mathbf{k} close to the nodes in the superconducting energy gap $\Delta(\mathbf{k})$ (116). This nodal quantum criticality is expected to lead to a peculiar $T^{3/2}$ -dependence of λ_L near the QCP. Such a T -dependence has been reported not only in $\text{BaFe}_2(\text{As}_{1-x}\text{P}_x)_2$ with x close to 0.3 but also in $\kappa\text{-(BEDT-TTF)}_2\text{Cu(NCS)}_2$ and CeCoIn_5 , which may also be close to a QCP.

4.3. Continuous Quantum Phase Transition Inside the Dome

The penetration-depth measurements provide clear and direct evidence of the presence of a QCP lying beneath the superconducting dome (74). This implies that the non-Fermi liquid behavior indicated by the red region in Figure 7a is most likely associated with the finite-temperature quantum critical region linked to the QCP. In addition, the enhanced quasiparticle mass implies that the Fermi energy is suppressed, which is usually less advantageous for high T_c . The fact that the highest T_c is nevertheless attained right at the QCP with the most enhanced mass strongly suggests that the quantum critical fluctuations help to enhance superconductivity in this system.

Moreover, this transition immediately indicates two distinct superconducting ground states. The strong temperature dependence of $\Delta\lambda(T)$ at low temperatures observed on both sides of the QCP argues against a drastic change in the superconducting gap structure (9, 117). The fact that the zero-temperature extrapolation of the AFM transition $T_N(x)$ into the dome coincides with the location of the QCP leads us to conclude that the QCP separates a pure superconducting phase and a superconducting phase coexisting with the SDW order (Figure 2c). The present results strongly suggest that superconductivity and SDW coexist on a microscopic level but compete for the same electrons in the underdoped region. This competition is evidenced by the overall larger $\lambda_L(0)$ values on the SDW side of the QCP than on the other side (Figure 4d), which might be explained by a smaller Fermi surface volume due to partial SDW gapping. The microscopic coexistence is also supported by the enhancement of $\lambda_L^2(0)$ as the QCP is approached from the SDW side, which is not expected in the case of phase separation.

We stress that the observed critical behavior of $\lambda_L(0)$ has never been reported in any other superconductors, including other iron-based (111, 118), heavy-fermion, and cuprate (61) superconductors. The doping evolution of $\lambda_L(0)$ has been reported in electron-doped $\text{Ba(Fe}_{1-x}\text{Co}_x)_2\text{As}_2$, but $\lambda_L(0)$ increases monotonically with decreasing x , and no special feature is observed even when crossing the magnetic phase boundary at $x \approx 0.06$. There are several possible reasons for this. First, recent neutron diffraction measurements on electron-doped $\text{Ba(Fe}_{1-x}\text{Ni}_x)_2\text{As}_2$ demonstrated that the commensurate static AFM order changes into transversely incommensurate

short-range AFM order near optimal superconductivity (119), implying that the first-order magnetic transition takes place in the phase diagram and that there is no QCP in the electron-doped compound, although there are some reports suggesting quantum critical behavior in the normal-state properties of $\text{Ba}(\text{Fe}_{1-x}\text{Co}_x)_2\text{As}_2$ (120–122). Second, the QCP anomaly may be smeared out by a greater degree of the electronic disorder that is caused by Co doping in the Fe planes. Thus, it remains unclear whether the long-range AFM order truly coexists microscopically with superconducting regions in electron-doped systems.

The microscopic coexistence of SDW and superconductivity is also supported by ^{31}P -NMR measurements in $\text{BaFe}_2(\text{As}_{1-x}\text{P}_x)_2$ with $x = 0.25$ (71). The magnetic moment of an Fe atom grows rapidly as the temperature is decreased below T_N , but it is seriously reduced when the system undergoes the superconducting transition at T_c , indicating a direct coupling between magnetic and superconducting order parameters. These results appear to indicate that the electrons on the same Fermi surfaces contribute to both magnetic ordering and unconventional superconductivity in $\text{BaFe}_2(\text{As}_{1-x}\text{P}_x)_2$. It should be noted that in the heavy-fermion compounds $\text{CeCo}(\text{In}_{1-x}\text{Cd}_x)_5$ and CeRhIn_5 , where T_N is higher than T_c , such a reduction is not observed. These results suggest that magnetism and superconductivity may emerge from different parts of the Fermi sheets in these heavy-fermion compounds, implying weak coupling between magnetism and superconductivity, which is consistent with the phase separation shown in **Figure 2b**. In cuprates, a QCP associated with the pseudogap formation has been discussed at the putative critical hole concentration $p_0 \sim 0.19$ inside the superconducting dome. It should be noted, however, that a broad minimum of $\lambda_L^2(0)$ reported in $\text{Bi}_2\text{Sr}_2\text{CaCu}_2\text{O}_{8+x}$ at p_0 (61) is in sharp contrast to the striking enhancement of $\lambda_L^2(0)$ in $\text{BaFe}_2(\text{As}_{1-x}\text{P}_x)_2$. Therefore, the nature of the QCP in cuprates, if present, may be very different from that found in iron pnictides.

4.4. Nematic Quantum Criticality

In iron pnictides, orbital physics and magnetism are highly entangled, which is similar to what is found in manganites, because of the strong interaction between spin and orbital motion (123). Closely related with this issue is the electronic nematicity, which is a unidirectional self-organized state that breaks the rotational symmetry of the underlying lattice. This nematicity and its relation to superconductivity have been an important issue in iron pnictides (14–30).

It has been suggested that the electronic nematicity in pnictides is associated with the tetragonal-to-orthorhombic structural transition. As the magnetic critical point at $x_c = 0.30$ is approached, the structural transition temperature T_s decreases along with the SDW ordering temperature. Therefore, the nematic fluctuations are expected to be enhanced near x_c (23, 25, 88). Indeed, the critical behavior of the nematic fluctuations have been reported in ultrasound (121) and the elastic response of resistivity anisotropy measurements (122) for $\text{Ba}(\text{Fe}_{1-x}\text{Co}_x)_2\text{As}_2$.

Recent magnetic torque experiments in $\text{BaFe}_2(\text{As}_{1-x}\text{P}_x)_2$ suggest that the electronic nematicity appears at a temperature T^* much higher than T_s and that the superconducting dome is covered under the T^* line (29). Moreover, very recent ARPES measurements show that the inequivalent energy shifts of the d_{xz} and d_{yz} bands, which have been observed in the AFM state below T_N (19, 20), seem to emerge at around this T^* line (124). At the same time, the DOS near the Fermi level shows a pseudogap-like depletion below T^* (124), which is also suggested from optical conductivity measurements (125). In addition, the NMR $1/T_1T$ becomes enhanced below T^* (126). Although further studies are necessary to clarify the nature of the electronic state changes at T^* and T_s , an interesting possibility is that ferro-orbital ordering occurs at T_s , whereas antiferro-orbital ordering takes place at T^* (25). In this case, the associated anomalies, which are clearly detected at T_s , may not be detected at T^* by long wavelength ($q \sim 0$) probes, such as elastic constants.

5. BARDEEN-COOPER-SCHRIEFFER-BOSE-EINSTEIN CONDENSATE CROSSOVER

The discovery of the QCP inside the dome illustrates another new aspect of the superconducting state in iron pnictides, which has never been realized in any of the other superconductors. In **Figure 8a**, T_c is plotted as a function of T_F in $\text{BaFe}_2(\text{As}_{1-x}\text{P}_x)_2$ for various x . Because the relevant Fermi surface sheets are nearly cylindrical, T_F may be estimated directly from the superfluid density $\lambda_L^{-2}(0)$ via the relation $T_F = (\hbar^2 \pi) n_{s2D} / k_B m^* \approx \hbar^2 \pi / \mu_0 e^2 d \lambda_L^2(0)$, where n_{s2D} is the carrier concentration within the superconducting planes and d is the interlayer spacing. The results of various superconductors are also shown in **Figure 8a**, where T_F is given by $T_F = (\hbar^2/2)(3\pi^2)^{2/3} n_s^{2/3} / k_B m^*$ for 3D systems (127). **Figure 8a** presents the Bose-Einstein condensation (BEC) temperature for an ideal 3D boson gas: $T_B = \frac{\hbar^2}{2\pi m^* k_B} \left(\frac{n_s}{2.612} \right)^{2/3} = 0.0176 T_F$.

In a quasi-2D system, this value of T_B provides an estimate of the maximum condensate temperature. The evolution of the superfluid density in the present system is in sharp contrast to that in cuprates, in which T_c is roughly scaled by T_F . **Figure 8b** depicts the P-composition dependence of T_c normalized by the Fermi (or BEC) temperature: T_c/T_F (T_c/T_B). In the large composition region ($x > 0.6$), T_c/T_F is very small, comparable to that of the conventional superconductor Nb. As x is decreased, T_c/T_F increases rapidly, and then decreases in the SDW region after reaching the maximum at the QCP ($x = 0.30$). What is remarkable is that the magnitude of T_c/T_B (≈ 0.30) at the

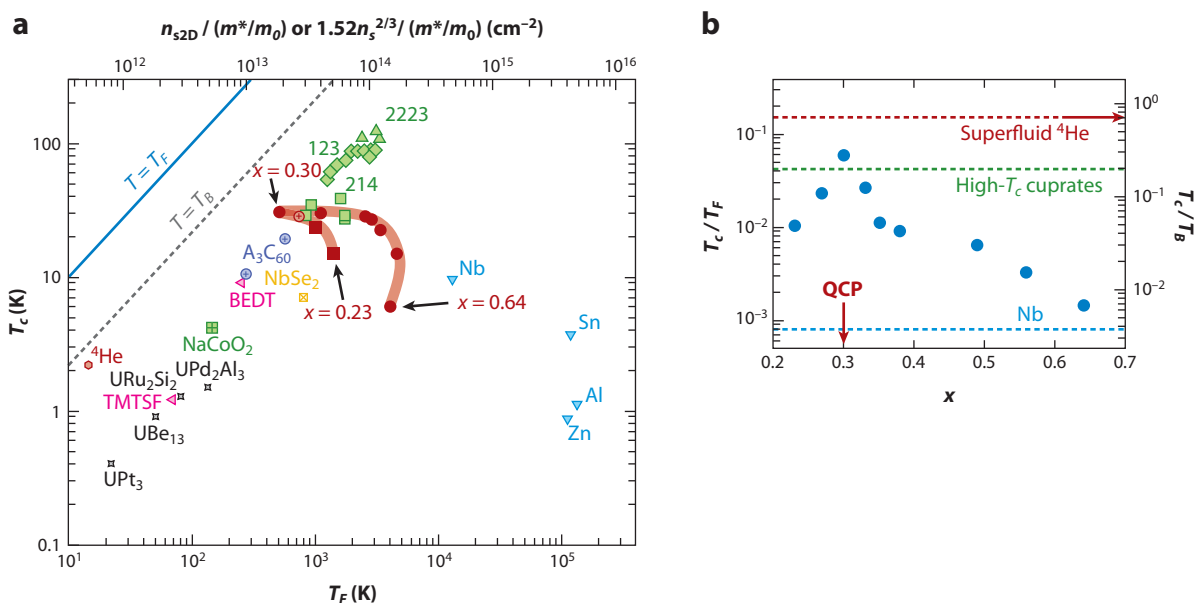


Figure 8

Comparisons between the superconducting transition temperature T_c and the effective Fermi temperature T_F (74). (a) The so-called Uemura plot, where T_c is plotted against T_F estimated from the superfluid density. The data for $\text{BaFe}_2(\text{As}_{1-x}\text{P}_x)_2$ with different x (red circles and lines) show a quite different behavior from the linear relation found for high- T_c cuprates and other exotic superconductors, and bridge the gap between conventional Bardeen-Cooper-Schrieffer superconductors and unconventional superconductors. The thick red lines guide the x dependence of T_c for $\text{BaFe}_2(\text{As}_{1-x}\text{P}_x)_2$. (b) T_c/T_F ratio as a function of x . The dashed lines represent typical values of T_c/T_F for Nb (blue) and cuprates (green), and T_c/T_B for superfluid ^4He (red). Abbreviation: QCP, quantum critical point.

QCP exceeds that of cuprates and reaches as large as nearly 40% of the value of superfluid ^4He . This sharp peak in T_c/T_F implies that the pairing interaction becomes strongest at the QCP and that the quantum critical fluctuations help to enhance superconductivity in this system.

6. CONCLUSIONS

In this review, we discussed the quantum criticality of iron-based high- T_c superconductors, addressing the issue of a QCP lying beneath the superconducting dome, which we believe to be crucially important for the understanding of anomalous non-Fermi liquid properties, microscopic coexistence between superconductivity and magnetic order, and the mechanism of superconductivity. In cuprates and heavy-fermion compounds, this issue, i.e., whether the pseudogap phase in cuprates and the SDW phase in heavy-fermion compounds terminate at a QCP deep inside the dome, has been hotly debated but remains puzzling.

We have shown that the isovalent doped pnictide $\text{BaFe}_2(\text{As}_{1-x}\text{P}_x)_2$ is an ideal system to study this issue because we can tune the electronic properties through a wide range of the phase diagram, ranging from SDW metal, through high- T_c superconductor, to conventional Fermi liquid metal, without introducing appreciable scattering. The transport properties, NMR, quantum oscillations, and specific heat all suggest the presence of the QCP at $x_c = 0.30$. Moreover, zero-temperature London penetration-depth measurements provide clear and direct evidence of the QCP lying beneath the superconducting dome. The QCP inside the dome includes the following important implications:

1. The QCP is the origin of the non-Fermi liquid behavior above T_c .
2. Unconventional superconductivity coexists with a SDW antiferromagnetism on a microscopic level.
3. The quantum critical fluctuations help to enhance the high- T_c superconductivity.

The presence or absence of a QCP inside the dome is still a question of debate not only in cuprates and heavy fermions but also in other pnictides. With three unconventional superconducting systems to compare and contrast, the vital clues that could be used to solve the mystery of anomalous electronic properties and unconventional superconductivity might be uncovered.

DISCLOSURE STATEMENT

The authors are not aware of any affiliations, memberships, funding, or financial holdings that might be perceived as affecting the objectivity of this review.

ACKNOWLEDGMENTS

The authors acknowledge collaborations with A.F. Bangura, A.E. Böhmer, K. Cho, A.I. Coldea, H. Eisaki, A. Fujimori, H. Fukazawa, R.W. Giannetta, K. Hashimoto, H. Ikeda, S. Kasahara, H. Kitano, K. Ishida, T. Iye, A. Iyo, L. Malone, C. Meingast, Y. Mizukami, Y. Nakai, K. Okazaki, C. Proust, R. Prozorov, C. Putzke, N. Salovich, T. Shimojima, S. Shin, H. Shishido, M.A. Tanatar, T. Terashima, S. Tonegawa, M. Yamashita, D. Vignolles, P. Walmsley, D. Watanabe, and T. Yoshida. We also thank the following for helpful discussions: E. Abrahams, R. Arita, A.V. Chubukov, I. Eremin, D.L. Feng, R.M. Fernandes, T. Hanaguri, P.J. Hirschfeld, H. Kontani, K. Kuroki, I.I. Mazin, S. Sachdev, J. Schmalian, Q. Si, T. Tohyama, Y.J. Uemura, S. Uchida, and H.H. Wen.

LITERATURE CITED

1. Kamihara Y, Hiramatsu H, Hirano M, Kawamura R, Yanagi H, et al. 2006. *J. Am. Chem. Soc.* 128:10012–13
2. Kamihara Y, Watanabe T, Hirano M, Hosono H. 2008. *J. Am. Chem. Soc.* 130:3296–97
3. Takahashi H, Igawa K, Aii K, Kamihara Y, Hirano M, Hosono H. 2008. *Nature* 453:376–78
4. Wang C, Li L, Chi S, Zhu Z, Ren Z, et al. 2008. *Europhys. Lett.* 83:67006
5. Ishida K, Nakai Y, Hosono H. 2009. *J. Phys. Soc. Jpn.* 78:062001
6. Paglione J, Greene RL. 2010. *Nat. Phys.* 6:645–58
7. Stewart GR. 2011. *Rev. Mod. Phys.* 83:1589–652
8. Mazin II. 2010. *Nature* 464:183–86
9. Hirschfeld PJ, Korshunov MM, Mazin II. 2011. *Rep. Prog. Phys.* 74:124508
10. Wen H-H, Li S. 2011. *Annu. Rev. Condens. Matter Phys.* 2:121–40
11. Chubukov A. 2012. *Annu. Rev. Condens. Matter Phys.* 3:57–92
12. Scalapino DJ. 1995. *Phys. Rep.* 250:329–65
13. Pfleiderer C. 2009. *Rev. Mod. Phys.* 81:1551–624
14. Yildirim T. 2009. *Physica C* 469:425–41
15. Lee C-C, Yin W-G, Ku W. 2009. *Phys. Rev. Lett.* 103:267001
16. Chen C-C, Maciejko J, Sorini AP, Moritz B, Singh RRP, Devereaux TP. 2010. *Phys. Rev. B* 82:100504 (R)
17. Chuang T-M, Allan MP, Lee J, Xie Y, Ni N, et al. 2010. *Science* 327:181–84
18. Chu J-H, Analytis JG, De Greve K, McMahon PL, Islam Z, et al. 2010. *Science* 329:824–26
19. Shimojima T, Ishizaka K, Ishida Y, Katayama N, Ohgushi K, et al. 2010. *Phys. Rev. Lett.* 104:057002
20. Yi M, Lu D, Chu J-H, Analytis JG, Sorini AP, et al. 2011. *Proc. Natl. Acad. Sci. USA* 108:6878–83
21. Kim YK, Jung WS, Han GR, Choi K-Y, Kim K-H, et al. 2011. arXiv:1112.2243
22. Fernandes RM, Abrahams E, Schmalian J. 2011. *Phys. Rev. Lett.* 107:217002
23. Fernandes RM, Chubukov AV, Knolle J, Eremin I, Schmalian J. 2012. *Phys. Rev. B* 85:024534
24. Fernandes RM, Schmalian J. 2012. *Supercond. Sci. Technol.* 25:084005
25. Kontani H, Onari S. 2011. *Phys. Rev. B* 84:024528
26. Onari S, Kontani H. 2012. *Phys. Rev. B* 85:134507
27. Bascones E, Valenzuela B, Calderon MJ. 2012. *Phys. Rev. B* 86:174508
28. Lee W-C, Phillips PW. 2012. *Phys. Rev. B* 86:245113
29. Kasahara S, Shi HJ, Hashimoto K, Tonegawa S, Mizukami Y, et al. 2012. *Nature* 486:382–85
30. Blomberg EC, Tanatar MA, Fernandes RM, Mazin II, Shen B, et al. 2013. *Nat. Commun.* 4:1914
31. Timusk T, Statt B. 1999. *Rep. Prog. Phys.* 62:61–122
32. He R-H, Hashimoto M, Karapetyan H, Koralek DJ, Hinton JP, et al. 2010. *Science* 331:1579–83
33. Vishik IM, Hashimoto M, He R-H, Lee W-S, Schmitt F, et al. 2012. *Proc. Natl. Acad. Sci. USA* 109:18332–37
34. Lawler MJ, Fujita K, Lee J, Schmidt AR, Kohsaka Y, et al. 2010. *Nature* 466:347–52
35. Daou R, Chang J, LeBoeuf D, Cyr-Choinière O, Laliberté F, et al. 2010. *Nature* 463:519–22
36. Fauqué B, Sidis Y, Hinkov V, Pailhès S, Lin CT, et al. 2006. *Phys. Rev. Lett.* 96:197001
37. Xia J, Schemm E, Deutscher G, Kivelson SA, Bonn DA, et al. 2008. *Phys. Rev. Lett.* 100:127002
38. Wu T, Mayaffre H, Krämer S, Horvatić M, Berthier C, et al. 2011. *Nature* 477:191–94
39. Kuramoto Y, Kusunose H, Kiss A. 2009. *J. Phys. Soc. Jpn.* 78:072001
40. Dai P, Hu J, Dagotto E. 2012. *Nat. Phys.* 8:709–18
41. Sachdev S. 2011. *Quantum Phase Transitions*. Cambridge: Cambridge Univ. Press
42. Vojta M. 2003. *Rep. Prog. Phys.* 66:2069–110
43. Sachdev S, Keimer B. 2011. *Phys. Today* 64:29–35
44. Sondhi SL, Girvin SM, Carini JP, Shahar D. 1997. *Rev. Mod. Phys.* 69:315–33
45. Varma CM, Nussinov Z, van Saarloos W. 2002. *Phys. Rep.* 361:267–417
46. von Löhneysen H, Rosch A, Vojta M, Wölfle P. 2007. *Rev. Mod. Phys.* 79:1015–75
47. Abrahams E, Si Q. 2011. *J. Phys. Condens. Matter* 23:223201

48. Coleman P, Schofield AJ. 2005. *Nature* 433:226–29
49. Broun DM. 2008. *Nat. Phys.* 4:170–72
50. Park T, Ronning F, Yuan HQ, Salamon MB, Movshovich R, et al. 2006. *Nature* 440:65–68
51. Knebel G, Aoki D, Braithwaite D, Salce B, Flouquet J. 2006. *Phys. Rev. B* 74:020501
52. Kasahara S, Shibauchi T, Hashimoto K, Ikada K, Tonegawa S, et al. 2010. *Phys. Rev. B* 81:184519
53. Shishido H, Bangura AF, Coldea AI, Tonegawa S, Hashimoto K, et al. 2010. *Phys. Rev. Lett.* 104:057008
54. van der Beek CJ, Konczykowski M, Kasahara S, Terashima T, Okazaki R, et al. 2010. *Phys. Rev. Lett.* 105:267002
55. Si Q, Steglich F. 2010. *Science* 329:1161–66
56. Gegenwart P, Si Q, Steglich F. 2008. *Nat. Phys.* 4:186–97
57. Moriya T, Ueda K. 2000. *Adv. Phys.* 49:555–606
58. Schröder A, Aeppli G, Coldea R, Adams M, Stockert O, et al. 2000. *Nature* 407:351–55
59. Custers J, Gegenwart P, Wilhelm H, Neumaier K, Tokiwa Y, et al. 2003. *Nature* 424:524–27
60. Borzi RA, Grigera SA, Farrell J, Perry RS, Lister SJS, et al. 2007. *Science* 315:214–17
61. Tallon JL, Loram JW, Cooper JR, Panagopoulos C, Bernhard C. 2003. *Phys. Rev. B* 68:180501
62. Ghiringhelli G, Le Tacon M, Minola M, Blanco-Canosa S, Mazzoli S, et al. 2012. *Science* 337:821–25
63. Chang J, Blackburn E, Holmes AT, Christensen NB, Larsen J, et al. 2012. *Nat. Phys.* 8:871–76
64. Vignolle B, Vignolles D, LeBoeuf D, Lepault S, Ramshaw B, et al. 2011. *C. R. Phys.* 12:446–60
65. Sebastian SE, Harrison N, Altarawneh MM, Mielke CH, Liang RX, et al. 2010. *Proc. Natl. Acad. Sci. USA* 107:6175–79
66. Kawasaki S, Mito T, Kawasaki Y, Zheng G-Q, Kitaoka Y, et al. 2003. *Phys. Rev. Lett.* 91:137001
67. Kawasaki S, Mito T, Kawasaki Y, Kotegawa H, Zheng G-Q, et al. 2004. *J. Phys. Soc. Jpn.* 73:1647–50
68. Pratt DK, Tian W, Kreyssig A, Zarestky JL, Nandi S, et al. 2009. *Phys. Rev. Lett.* 103:087001
69. Christianson AD, Lumsden MD, Nagler SE, MacDougall GJ, McGuire MA, et al. 2009. *Phys. Rev. Lett.* 103:087002
70. Wang M, Luo H, Wang M, Chi S, Rodriguez-Rivera JA, et al. 2011. *Phys. Rev. B* 83:094516
71. Iye T, Nakai Y, Kitagawa S, Ishida K, Kasahara S, et al. 2012. *Phys. Rev. B* 85:184505
72. Iye T, Nakai Y, Kitagawa S, Ishida K, Kasahara S, et al. 2012. *J. Phys. Soc. Jpn.* 81:033701
73. Thalmeier P, Zwicky G. 2005. *Handb. Phys. Chem. Rare Earths* 34:135–287
74. Hashimoto K, Cho K, Shibauchi T, Kasahara S, Mizukami Y, et al. 2012. *Science* 336:1554–57
75. Wen H-H. 2012. *Rep. Prog. Phys.* 75:112501
76. Matan K, Morinaga R, Iida K, Sato TJ. 2009. *Phys. Rev. B* 79:054526
77. Bao W, Qiu Y, Huang Q, Green MA, Zajdel P, et al. 2009. *Phys. Rev. Lett.* 102:247001
78. Malaeb W, Shimojima T, Ishida Y, Okazaki K, Ota Y, et al. 2012. *Phys. Rev. B* 86:165117
79. Nakayama K, Sato T, Richard P, Xu Y-M, Kawahara T, et al. 2011. *Phys. Rev. B* 83:020501 (R)
80. Analytis JG, Chu J-H, McDonald RD, Riggs SC, Fisher IR. 2010. *Phys. Rev. Lett.* 105:207004
81. Arnold BJ, Kasahara S, Coldea AI, Terashima T, Matsuda Y, et al. 2011. *Phys. Rev. B* 83:220504 (R)
82. Walmsley P, Putzke C, Malone L, Guillamon I, Vignolles D, et al. 2013. *Phys. Rev. Lett.* 110:257002
83. Mazin II, Singh DJ, Johannes MD, Du MH. 2008. *Phys. Rev. Lett.* 101:057003
84. Kuroki K, Usui H, Onari S, Arita R, Aoki H. 2009. *Phys. Rev. B* 79:224511
85. Graser S, Maier TA, Hirschfeld PJ, Scalapino DJ. 2009. *New J. Phys.* 11:025016
86. Ikeda H, Arita R, Kuneš J. 2010. *Phys. Rev. B* 81:054502
87. Kontani H, Onari S. 2010. *Phys. Rev. Lett.* 104:157001
88. Onari S, Kontani H. 2012. *Phys. Rev. Lett.* 109:137001
89. Thomale R, Platt C, Hanke W, Hu J, Bernevig BA. 2011. *Phys. Rev. Lett.* 107:117001
90. Tanatar MA, Reid J-P, Shakeripour H, Luo XG, Doiron-Leyraud N, et al. 2010. *Phys. Rev. Lett.* 104:067002
91. Hashimoto K, Shibauchi T, Kasahara S, Ikada K, Tonegawa S, et al. 2010. *Phys. Rev. Lett.* 102:207001
92. Ding H, Richard P, Nakayama K, Sugawara K, Arakane T, et al. 2008. *Europhys. Lett.* 83:47001
93. Fukazawa H, Yamada Y, Kondo K, Saito T, Kohori Y, et al. 2009. *J. Phys. Soc. Jpn.* 78:083712
94. Dong JK, Zhou SY, Guan TY, Zhang H, Dai YF, et al. 2010. *Phys. Rev. Lett.* 104:087005
95. Hashimoto K, Serafin A, Tonegawa S, Katsumata R, Okazaki R, et al. 2010. *Phys. Rev. B* 82:014526

96. Reid J-P, Tanatar MA, Juneau-Fecteau A, Gordon RT, de Cotret SR, et al. 2012. *Phys. Rev. Lett.* 109:087001
97. Okazaki K, Ota Y, Kotani Y, Malaeb W, Ishida Y, et al. 2012. *Science* 337:1314–17
98. Hashimoto K, Yamashita M, Kasahara S, Senshu Y, Nakata N, et al. 2010. *Phys. Rev. B* 81:220501 (R)
99. Yamashita M, Senshu Y, Shibauchi T, Kasahara S, Hashimoto K, et al. 2011. *Phys. Rev. B* 84:060507 (R)
100. Wang Y, Kim JS, Stewart GR, Hirschfeld PJ, Graser S, et al. 2011. *Phys. Rev. B* 84:184524
101. Shimojima T, Sakaguchi F, Ishizaka K, Ishida Y, Kiss T, et al. 2011. *Science* 332:564–67
102. Yoshida T, Ideta S, Shimojima T, Malaeb W, Shinada K, et al. 2013. arXiv:1301.4818
103. Zhang Y, Ye ZR, Ge QQ, Chen F, Jiang J, et al. 2012. *Nat. Phys.* 8:371–75
104. Mishra V, Boyd G, Graser S, Maier T, Hirschfeld PJ, Scalapino DJ. 2009. *Phys. Rev. B* 79:094512
105. Dai J, Si Q, Zhu J-X, Abrahams E. 2009. *Proc. Natl. Acad. Sci. USA* 106:4118–21
106. Nakajima Y, Shishido H, Nakai H, Shibauchi H, Behnia K, et al. 2007. *J. Phys. Soc. Jpn.* 76:024703
107. Nakai Y, Iye T, Kitagawa S, Ishida K, Ikeda H, et al. 2010. *Phys. Rev. Lett.* 105:107003
108. Yoshida T, Nishi I, Ideta S, Fujimori A, Kubota M, et al. 2011. *Phys. Rev. Lett.* 106:117001
109. Chaparro C, Fang L, Claus H, Rydh A, Crabtree GW, et al. 2012. *Phys. Rev. B* 85:184525
110. Prozorov R, Giannetta RW, Carrington A, Fournier P, Greene RL. 2000. *Appl. Phys. Lett.* 77:4202–4
111. Gordon RT, Kim H, Salovich N, Giannetta RW, Fernandes RM, et al. 2010. *Phys. Rev. B* 82:054507
112. Leggett AJ. 1965. *Phys. Rev.* 140:A1869–88
113. Levchenko A, Vavilov MG, Khodas M, Chubukov AV. 2012. *Phys. Rev. Lett.* 110:177003
114. Nomoto T, Ikeda H. 2013. *Phys. Rev. Lett.* 111:157004
115. Chowdhury D, Swingle B, Berg E, Sachdev S. 2013. arXiv:1305.2918 [cond-mat.str-el]
116. Hashimoto K, Mizukami Y, Katsumata R, Shishido H, Yamashita M, et al. 2013. *Proc. Natl. Acad. Sci. USA* 110:3293–97
117. Fernandes RM, Schmalian J. 2010. *Phys. Rev. B* 82:014520
118. Luan L, Lippman TM, Hicks CW, Bert JA, Auslaender OM, et al. 2011. *Phys. Rev. Lett.* 106:067001
119. Luo H, Zhang R, Laver M, Yamani Z, Wang M, et al. 2012. *Phys. Rev. Lett.* 108:247002
120. Ning FL, Ahilan K, Imai T, Sefat AS, McGuire MA, et al. 2010. *Phys. Rev. Lett.* 104:037001
121. Yoshizawa M, Kimura D, Chiba T, Simayi S, Nakanishi Y, et al. 2012. *J. Phys. Soc. Jpn.* 81:024604
122. Chu J-H, Kuo H-H, Analytis JG, Fisher IR. 2012. *Science* 337:710–12
123. Kugel KI, Khomskii DI. 1973. *Sov. Phys. JETP* 37:725–30
124. Shimojima T, Sonobe T, Malaeb W, Shinada K, Chainani A, et al. 2013. *Phys. Rev. B*. In press
125. Moon SJ, Schafgans AA, Kasahara S, Shibauchi T, Terashima T, et al. 2012. *Phys. Rev. Lett.* 109:027006
126. Nakai Y, Iye T, Kitagawa S, Ishida K, Kasahara S, et al. 2013. *Phys. Rev. B* 87:174507
127. Uemura YJ. 2004. *J. Phys. Condens. Matter* 16:S4515–40
128. Watanabe D, Yamashita T, Kawamoto Y, Kurata S, Mizukami Y, et al. 2013. arXiv:1307.3408



Contents

Whatever Happened to Solid State Physics? <i>John J. Hopfield</i>	1
Noncentrosymmetric Superconductors <i>Sungkit Yip</i>	15
Challenges and Opportunities for Applications of Unconventional Superconductors <i>Alex Gurevich</i>	35
Correlated Quantum Phenomena in the Strong Spin-Orbit Regime <i>William Witczak-Krempa, Gang Chen, Yong Baek Kim, and Leon Balents</i>	57
Dirac Fermions in Solids: From High- T_c Cuprates and Graphene to Topological Insulators and Weyl Semimetals <i>Oskar Vafek and Ashvin Vishwanath</i>	83
A Quantum Critical Point Lying Beneath the Superconducting Dome in Iron Pnictides <i>T. Shibauchi, A. Carrington, and Y. Matsuda</i>	113
Hypercomplex Liquid Crystals <i>Zvonimir Dogic, Prerna Sharma, and Mark J. Zakhary</i>	137
Exciton Condensation in Bilayer Quantum Hall Systems <i>J.P. Eisenstein</i>	159
Bird Flocks as Condensed Matter <i>Andrea Cavagna and Irene Giardina</i>	183
Crossover from Bardeen-Cooper-Schrieffer to Bose-Einstein Condensation and the Unitary Fermi Gas <i>Mohit Randeria and Edward Taylor</i>	209

Crackling Noise in Disordered Materials <i>Ekhard K.H. Salje and Karin A. Dahmen</i>	233
Growing Length Scales and Their Relation to Timescales in Glass-Forming Liquids <i>Smarajit Karmakar, Chandan Dasgupta, and Srikanth Sastry</i>	255
Multicarrier Interactions in Semiconductor Nanocrystals in Relation to the Phenomena of Auger Recombination and Carrier Multiplication <i>Victor I. Klimov</i>	285
Polycrystal Plasticity: Comparison Between Grain-Scale Observations of Deformation and Simulations <i>Reeju Pokharel, Jonathan Lind, Anand K. Kanjarla, Ricardo A. Lebensohn, Shiu Fai Li, Peter Kenesei, Robert M. Suter, and Anthony D. Rollett</i>	317
Molecular Beam Epitaxy of Ultra-High-Quality AlGaAs/GaAs Heterostructures: Enabling Physics in Low-Dimensional Electronic Systems <i>Michael J. Manfra</i>	347
Simulations of Dislocation Structure and Response <i>Richard LeSar</i>	375

Errata

An online log of corrections to *Annual Review of Condensed Matter Physics* articles may be found at <http://www.annualreviews.org/errata/conmatphys>